POLITECNICO DI TORINO
Repository ISTITUZIONALE

Temperature and degree of cure 3D distributions in fiber-reinforced and sandwich composites using 1D finite elements

*Original*
Temperature and degree of cure 3D distributions in fiber-reinforced and sandwich composites using 1D finite elements / Zappino, E., Santori, M., Zobeiry, N., Petrolo, M.. - In: MECHANICS OF MATERIALS. - ISSN 0167-6636. - ELETTRONICO. - 217:(2026). [10.1016/j.mechmat.2026.105651]

*Availability:*
This version is available at: 11583/3008435 since: 2026-11-10T08:22:47Z

*Publisher:*
Elsevier

*Published*
DOI:10.1016/j.mechmat.2026.105651

*Terms of use:*

This article is made available under terms and conditions as specified in the corresponding bibliographic description in the repository

*Publisher copyright*

(Article begins on next page)

13 November 2026

Mechanics of Materials 217 (2026) 105651

Contents lists available at ScienceDirect

Mechanics of Materials

journal homepage: www.elsevier.com/locate/mecmat

Research paper

# Temperature and degree of cure 3D distributions in fiber-reinforced and sandwich composites using 1D finite elements

E. Zappino [a,1], M. Santori [a,2], N. Zobeiry [b,1], M. Petrolo [a,*,1]

[a] MUL2 Lab, Department of Mechanical and Aerospace Engineering, Politecnico di Torino, Torino, Italy
[b] Materials Science & Engineering Department, University of Washington, Seattle, USA

ARTICLE INFO

Invited Editor Ghatu Subhash

*Keywords:*
Virtual manufacturing
Multifield analysis
Composites
Sandwich structures

ABSTRACT

This paper presents a multifield numerical approach to analyze the thermochemical behavior of composite structures during curing. A 1D high-fidelity model, developed within the Carrera Unified Formulation (CUF) and the Finite Element Method (FEM), is employed to solve the coupled heat-transfer and cure-kinetics equations. This approach allows accurate prediction of both temperature and degree of cure during the curing cycle, providing full 3D distributions for these variables. The modeling approach is layer-wise (LW), with each ply explicitly modeled and having a set of unknown variables. The proposed methodology is applied to graphite/epoxy composite laminates and extended to a hybrid solid laminate/honeycomb structure, demonstrating its applicability to both monolithic and complex structures. The influence of different boundary conditions, such as temperature and free-surface convection, and non-homogeneous convection, is analyzed. The results consider the time evolution of temperature and degree of cure, and the 3D distribution within the composite part. The model's accuracy is verified through results from the literature.

## 1. Introduction

Carbon Fiber Reinforced Polymers (CFRP) have gained more interest in recent years in the aerospace industry due to their high strength-to-weight ratio and excellent mechanical properties compared to traditional metallic materials (Baker and Scott, 2016). These materials are also widely used in complex structural configurations such as sandwich panels, which typically consist of two thin skins with high elastic modulus and a thick core with lower density. This configuration provides the structure with high bending stiffness while allowing for significant weight reduction, making it suitable for high-performance applications (Leijten et al., 2009; Belingardi et al., 2003).

Despite these advantages, large-scale adoption of CFRPs remains limited, primarily due to the complexity of their manufacturing processes. The autoclave process is influenced by different parameters, including geometry, material properties, setup, and tool-part interaction (Wang et al., 2023; Zappino et al., 2024b). Therefore, an accurate understanding of these aspects and their impact on the final performance is essential to ensure the components are of high quality.

During curing, the composite part is subjected to high temperature and pressure cycles to induce an exothermic chemical reaction in the resin (Fernlund et al., 2018). The polymerization cross-links at the microscopic level in the resin, which enhances the mechanical properties, such as stiffness, and reduces voids (Stringer, 1989). However, this transformation from a viscous liquid to a rigid solid may also introduce several defects, including non-uniform and incomplete polymerization, and the development of residual stresses and deformations, all of which affect the final quality of the component (Li et al., 2025).

At the microscopic level, the mismatch between the fiber and matrix thermal expansion coefficients and the volumetric shrinkage caused by the chemical reaction in the matrix, i.e., the chemical shrinkage, generate residual stresses in the composite part (Zobeiry and Poursartip, 2015; Maréchal et al., 2025). Additional factors can affect the final performance at the macroscopic level. For example, tool expansion under high temperature generates tensile stresses at the tool-part interface, which are partially released upon demolding and manifest as permanent shape distortions (Twigg et al., 2004a,b). The geometry of the part can also affect these defects. Curved sections, such as U or L-shaped, are more susceptible to flange deformation during demolding (Traiforos et al., 2023).

In sandwich structures, the presence of different materials with distinct thermomechanical properties further increases the complexity

* Correspondence to: MUL[2] Lab, Department of Mechanical and Aerospace Engineering, Politecnico di Torino, Corso Duca degli Abruzzi 24, 10129 Torino, Italy.
*E-mail addresses:* enrico.zappino@polito.it (E. Zappino), martina.santori@polito.it (M. Santori), navidz@uw.edu (N. Zobeiry), marco.petrolo@polito.it (M. Petrolo).
[1] Associate Professor.
[2] PhD Student

https://doi.org/10.1016/j.mechmat.2026.105651
Received 4 November 2025; Received in revised form 23 January 2026; Accepted 26 February 2026
Available online 5 March 2026
0167-6636/© 2026 The Authors. Published by Elsevier Ltd. This is an open access article under the CC BY-NC-ND license (http://creativecommons.org/licenses/by-nc-nd/4.0/).

of the curing process. Consequently, the cure cycle may need to be adapted to the specific hybrid configuration to ensure appropriate temperature and cure distributions (Johnston, 1997). Numerical simulations can therefore be used to design and optimize cure cycles that account for the different material requirements.

Numerous studies have been carried out in recent years on the simulation of the curing process (Mezeix et al., 2015; Chen and Zhang, 2019). Loos and Springer (1983) analyzed the curing process of flat plate composites and proposed a model for predicting temperature distribution, degree of cure, resin viscosity, void formation, internal pressures, and residual stress distribution. Bogetti and Gillespie (1992) and Bogetti (1989) presented a model for predicting process-induced strains and stresses. They developed a one-dimensional model to provide temperature along the thickness, cure-dependent mechanical properties, shrinkage, and thermal expansion deformations. White and Hahn (1992a,b) introduced a process model that predicts the evolution of residual stresses in composites during the curing process, considering the effects of thermal gradients and chemical shrinkage, and assuming linear and viscoelastic material behavior. More recently, some studies have been conducted on sandwich structures (Al-Dhaheri et al., 2020; Kappel, 2015).

Finite elements (FE) are commonly used for simulating the curing process and evaluating the effect of process parameters on performance (Johnston et al., 2001; Ersoy et al., 2010b,a; Fernlund et al., 2003). Johnston et al. (2001) developed a 2D FE model to predict deformations in laminated composites caused by manufacturing processes. The Cure Hardening Instantaneous Linear Elastic (CHILE) model was used to represent the mechanical behavior of the composite part. Zhu et al. (2001) developed a 3D coupled thermo-chemo viscoelastic model to simulate heat transfer, curing, residual stresses, and deformation of composites. Ersoy et al. (2010b) developed a 2D model to predict stress and spring-in, considering two phases, the rubbery and glassy states of the resin. Qiao and Yao (2020) included the tool-part interaction in the FE model to study the process-induced deformation. Given the complexity of the process, high-fidelity 3D FE methods are often necessary to ensure sufficient accuracy of the results. However, this approach is not always applicable, given the high computational cost and long simulation times. Even an experimental approach based on trial and error is not always cost-effective and can lead to material waste (Fernlund et al., 2002).

The present work aims to demonstrate the accuracy and potential of a higher-order one-dimensional FE model developed using the Carrera Unified Formulation (CUF). Governing equations are obtained using a compact form independent of the order of the structural theory (Carrera et al., 2014). The matrices and vectors involved in the weak form of governing equations are derived via fundamental nuclei, which are independent of the adopted theory. Refined CUF 1D models offer high fidelity and reduced computational costs. Previous work has shown the possibility of detecting 3D effects with a significantly lower number of degrees of freedom than conventional 2D/3D models (Carrera et al., 2021; Zappino et al., 2020). Recently, CUF models have been used to determine deformations and stresses induced by the curing process (Zappino et al., 2020, 2024a; Schoenholz et al., 2024; Nagaraj et al., 2024). In these studies, however, the CUF was used exclusively to model the structural response, while the thermochemical evolution was either prescribed from external analyses or incorporated as an input to the process model. Later, Nagaraj et al. (2024) introduced a higher-order CUF-based model for the process modeling of thermoset composites and validated it through experimental measurements and benchmark comparisons with reference 3D FE analyses; CUF is used to solve the thermal field and the mechanical response. The curing state, instead, is introduced through time integration of the cure kinetics to update the local material state during the process simulation. Conversely, the present work focuses on coupled thermochemical analysis, in which temperature and degree of cure are the primary variables; in other words, the present article shows, for the first time, the extension of CUF to a coupled thermochemical formulation in which both temperature and degree of cure are described using higher-order expansions across the cross-section. Despite using a 1D model, this approach obtains 3D distributions of temperature and degree of cure over the composite part. The main advantage of this model is its ability to assess the impact of non-uniform temperature fields on the behavior of composite and sandwich structures. This work, therefore, represents the first step toward verifying the proposed thermochemical model, with the ultimate goal of coupling it with the mechanical response. This paper is organized as follows: Section 2 describes the numerical model adopted in this work, including the derivation of the thermochemical equations using CUF; Section 3 concerns the numerical results; Section 4 presents the conclusions.

## 2. Thermochemical model and numerical solution

This section introduces the thermochemical equations and its solution via the Galerkin's method. Then, the CUF is introduced to model the temperature and degree of cure distributions.

### 2.1. Thermochemical model

The curing process involves coupled thermal and chemical phenomena. Heat generation from the exothermic reaction interacts with heat transfer within the material, leading to gradients in temperature and degree of cure. Thermochemical modeling helps understand these interactions. The heat transfer equation, coupled with cure kinetics models, enables the prediction of temperature and degree of cure fields throughout the composite during the curing process.

The heat transfer equation describes the composite material's spatial and temporal temperature distribution. For an anisotropic material, it is expressed as (Bogetti, 1989):

$$\rho C_p \frac{\partial T}{\partial t} = \nabla \cdot \left( \boldsymbol{k} \nabla T \right) + \dot{Q} \tag{1}$$

$T$ is the temperature, $\nabla T$ is the gradient of temperature, and $t$ is the time. $\rho$ is the material density, $C_p$ is the specific heat, and $\boldsymbol{k}$ is the thermal conductivity tensor. Such thermal properties are considered constant and independent of temperature during the curing process. The term $\dot{Q}$ is the internal heat source, and it depends on the degree of cure, i.e.,

$$\dot{Q} = \rho H_r \frac{d\alpha}{dt} \tag{2}$$

$H_r$ is the composite's effective total heat of reaction and $\alpha$ is the degree of cure.

The cure kinetics governs the degree of cure time evolution. The cure rate is typically modeled using an Arrhenius-based approach combined with reaction order terms, and it can be expressed as:

$$\frac{d\alpha}{dt} = f(\alpha, T) \tag{3}$$

$f(\alpha, T)$ is a function of temperature and degree of cure and depends on the material of the composite part. For graphite/epoxy composites made of 3501-6 epoxy resin reinforced with AS4 carbon fibers, the model proposed by Bogetti and Gillespie is (Bogetti and Gillespie, 1992):

$$\begin{aligned} \frac{d\alpha}{dt} &= (k_1 + k_2\alpha)(1-\alpha)(0.47-\alpha) \quad && \text{for } (\alpha \leq 0.3) \\ \frac{d\alpha}{dt} &= k_3(1-\alpha) && \text{for } (\alpha > 0.3) \end{aligned} \tag{4}$$

$k_1$, $k_2$, and $k_3$ are the parameters defined by the following Arrhenius equation:

$$k_i = A_i e^{\frac{-\Delta E_i}{RT}} \qquad \text{for } i = 1, 2, 3 \tag{5}$$

The pre-exponential coefficients are denoted by $A_i$ and the activation energies by $E_i$. R is the universal gas constant. The numerical values of

**Table 1**
Cure kinetics parameters for AS4/3501-6 and AS4/8552.

| AS4/3501-6 | |
|---|---|
| $A_1$ (1/s) | $3.502 \times 10^7$ |
| $A_2$ (1/s) | $-3.357 \times 10^7$ |
| $A_3$ (1/s) | $3.267 \times 10^3$ |
| $\Delta E_1$ (J/mol) | $8.07 \times 10^4$ |
| $\Delta E_2$ (J/mol) | $7.78 \times 10^4$ |
| $\Delta E_3$ (J/mol) | $5.66 \times 10^4$ |
| $H_r$ (kJ/kg) | 198.9 |
| **AS4/8552** | |
| $m$ | 0.813 |
| $n$ | 2.74 |
| $A$ (1/s) | $1.528 \times 10^5$ |
| $\Delta E$ (J/mol) | $6.65 \times 10^4$ |
| $C$ | 43.1 |
| $\alpha_{C0}$ | −1.684 |
| $\alpha_{CT}$ | $5.475 \times 10^{-3}$ |
| $H_r$ (kJ/kg) | 231.7 |

the parameters involved in the cure rate formula are listed in Table 1. For an AS4 carbon fiber-reinforced Hexcel 8552 resin, the cure kinetics model is described by (Johnston, 1997):

$$\frac{d\alpha}{dt} = \frac{K\alpha^m(1-\alpha^n)}{1+e^{C[\alpha-(\alpha_{C0}+\alpha_{CT}T)]}} \qquad K = Ae^{-\frac{\Delta E}{RT}} \tag{6}$$

Both kinetic models assume a locally homogeneous reaction governed by temperature, with constant kinetic parameters and without accounting for viscosity effects, and vitrification phenomena. In this work, resin viscosity plays a secondary role, as the analysis is limited to the thermochemical problem and does not address the mechanical response during curing. Although viscosity can influence the curing process and becomes particularly relevant in mechanical behavior before and during gelation, these aspects are beyond the scope of this study. Furthermore, in previous CUF-based studies on the mechanical response during curing (Zappino et al., 2020), the effects of viscosity were also neglected by adopting the CHILE approach, which assumes negligible viscous behavior and has proven adequate for predicting the residual deformations induced by curing that develop after the gelation point. The same assumption is therefore consistently maintained in the present work. Furthermore, resin viscosity and flow-compaction effects are neglected, as the analysis focuses on the coupled thermo-chemical problem. Although flow compaction can alter ply thickness, which in turn may influence thermal diffusion and the degree of cure evolution, these thickness variations are secondary effects on temperature and degree of cure relative to the overall thickness of the part and tool assembly. Therefore, consistent with established modeling practices, cured ply thickness is used for thermo-chemical analysis, decoupled from flow-compaction analysis, see also Zobeiry et al. (2016).

### 2.2. FE formulation of thermochemical equations

The Galerkin method is employed to derive the FE formulation of the thermochemical model equations. The 3D domain, $V$, is divided into a finite set of elements, and within each element, "$e$", the temperature and degree of cure are approximated using interpolation functions:

$$T^e = v_m(x,y,z)T_m(t) \quad m=1,\dots,n \qquad \alpha^e = v_m(x,y,z)\alpha_m(t) \quad m=1,\dots,n \tag{7}$$

$v_m$ are the weight functions, and $T_m(t)$ and $\alpha_m(t)$ are the temperature and degree of cure at each element node, respectively. $n$ is the number of nodes in each element. According to the Einstein notation, the summation is carried out over the repeated subscript, $m$. Each equation of the thermochemical model - Eqs. (1) and (3) - is multiplied by $v_m$ and integrated over the domain, $V$,

$$\int_V \left(\rho C_p \frac{\partial T}{\partial t} v_m\right) dV = \int_V \nabla\cdot(\boldsymbol{k}\nabla T) v_m dV + \int_V \left(\rho H_r \frac{d\alpha}{dt} v_m\right) dV \tag{8}$$

The divergence theorem is applied in the second term of the equation:

$$\int_V \nabla\cdot(\boldsymbol{k}\nabla T) v_m dV = \int_S \Big((\boldsymbol{k}\nabla T)\cdot \boldsymbol{n} v_m\Big) dS - \int_V \Big((\boldsymbol{k}\nabla T)\cdot\nabla v_m\Big) dV \tag{9}$$

$\boldsymbol{n}$ is the normal vector to the boundary surface, $S$. The first term generated by applying the divergence theorem is related to the heat flow across $S$. If convection is applied, this term is the amount of heat that is transferred between the composite surface and the air in the autoclave and can be rewritten as:

$$\int_S \Big((\boldsymbol{k}\nabla T)\cdot \boldsymbol{n} v_m\Big) dS = \int_S \Big(h(T_\infty - T) v_m\Big) dS \tag{10}$$

$h$ is the heat transfer coefficient and $T_\infty$ is the temperature of the autoclave. Substituting Eq. (9) in Eq. (8), the following equation is obtained:

$$\int_V \left(\rho C_p \frac{\partial T}{\partial t} v_m\right) dV + \int_V \Big((\boldsymbol{k}\nabla T)\cdot\nabla v_m\Big) dV = \int_S \Big(h(T_\infty - T) v_m\Big) dS + \int_V \left(\rho H_r \frac{d\alpha}{dt} v_m\right) dV \tag{11}$$

Similarly, the Eq. (3) can be written in the following form:

$$\int_V \left(\frac{d\alpha}{dt} v_m\right) dV = \int_V \Big(f(\alpha,T) v_m\Big) dV \tag{12}$$

### 2.3. Carrera unified formulation

This paper adopts 1D theories to reduce the 3D problem and improve the computational efficiency and uses CUF to obtain the governing equations (Carrera et al., 2014). Fig. 1 shows the adopted reference system and, according to the CUF, the temperature and degree of cure fields can be written through an expansion function, $F_\tau$, over the cross-section:

$$T = F_\tau(x,z)T_\tau(y), \quad \tau=1,\dots,M \qquad \alpha = F_\tau(x,z)\alpha_\tau(y), \quad \tau=1,\dots,M \tag{13}$$

$T_\tau$ and $\alpha_\tau$ are the temperature and degree of cure unknowns along the beam axis, respectively. $M$ is the number of terms in the expansion. In this paper, Lagrange expansions are used. For example, if a biquadratic nine-node Lagrange element (LE9) is chosen to discretize the section, the temperature field can be approximated as follows:

$$T = L_1T_1 + L_2T_2 + L_3T_3 + L_4T_4 + L_5T_5 + L_6T_6 + L_7T_7 + L_8T_8 + L_9T_9 \tag{14}$$

where $L_i$ are the Lagrange polynomials. Along the $y$-direction, the structure is discretized into 1D finite elements, and four-node (B4) elements are used, leading to a cubic interpolation:

$$T = N_i(y)F_\tau(x,z)T_{i\tau}, \quad \tau=1,\dots,M;\ i=1,\dots,N_n \qquad \alpha = N_i(y)F_\tau(x,z)\alpha_{i\tau}, \quad \tau=1,\dots,M;\ i=1,\dots,N_n \tag{15}$$

$T_{i\tau}$ and $\alpha_{i\tau}$ are the nodal temperature and degree of cure unknowns, and $N_n$ is the number of nodes in each beam element. The use of higher-order CUF expansions throughout the section enables accurate prediction of temperature gradients and the degree of cure across the thickness. In the presence of strong in-plane gradients, the accuracy can be further enhanced by refining the FE discretization.

### 2.4. Thermochemical equations in CUF form

In CUF, the weight function $v_m$ becomes:

$$v_m(x,y,z) = N_j(y)F_s(x,z) \tag{16}$$

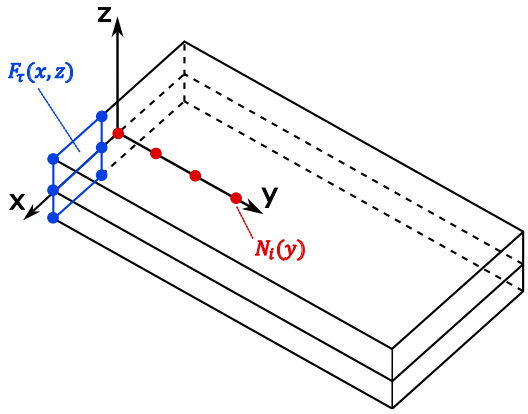



**Fig. 1.** 1D finite elements and CUF expansion functions.

By substituting $T$ and $\alpha$ - Eq. (15) - into Eqs. (11) and (12), the thermochemical equations take the following form:

$$\int_V \left(\rho C_p N_j F_s N_i F_\tau\right)\dot{T}dV + \int_V \left(\nabla N_j F_s k \nabla N_i F_\tau\right)T dV = \int_S \left(hN_j F_s(T_\infty - T)\right)dS + \int_V \left(\rho H_r N_j F_s N_i F_\tau\right)\dot{\alpha}dV \tag{17}$$

$$\int_V \left(N_j F_s N_i F_\tau\right)\dot{\alpha}dV = \int_V \left(N_i F_\tau g(\alpha,T)\right)dV \tag{18}$$

$(\cdot)$ indicates the time derivative. The thermochemical system in matrix form becomes:

$$\begin{bmatrix} D_T & D_{T\alpha} \\ 0 & D_\alpha \end{bmatrix}\begin{Bmatrix} \dot{T} \\ \dot{\alpha} \end{Bmatrix} + \begin{bmatrix} K_T & 0 \\ 0 & 0 \end{bmatrix}\begin{Bmatrix} T \\ \alpha \end{Bmatrix} = \begin{Bmatrix} P_T \\ P_\alpha \end{Bmatrix} \tag{19}$$

Each term's dimension is $1 \times 1$ and is written as fundamental nuclei:

- The thermal capacity term, $D_T$,

$$D_T = \int_L \int_A \left(\rho C_p N_i N_j F_\tau F_s\right)dA\,dL \tag{20}$$

- The thermal stiffness, $K_T$,

$$\begin{aligned} K_T = &\int_L \int_A \left(N_i N_j (\nabla_p^T F_s)\boldsymbol{\kappa}(\nabla_p F_\tau)\right)dA\,dL \\ &+ \int_L \int_A \left(N_j (\nabla_l N_i)\boldsymbol{\kappa}(\nabla_p^T F_s)F_\tau\right)dA\,dL \\ &+ \int_L \int_A \left((\nabla_l^T N_j)(N_i)\boldsymbol{\kappa}(\nabla_p F_\tau)F_s\right)dA\,dL \\ &+ \int_L \int_A \left((\nabla_l^T N_j)(\nabla_l N_i)F_\tau \boldsymbol{\kappa} F_s\right)dA\,dL \end{aligned} \tag{21}$$

  where $\nabla_l = \{\partial_x \;\; 0 \;\; \partial_z\}$ and $\nabla_n = \{0 \;\; \partial_y \;\; 0\}$.
- The curing heat source, $D_{T\alpha}$,

$$D_{T\alpha} = -\int_L \int_A \left(\rho H_r N_i N_j F_\tau F_s\right)dA\,dL \tag{22}$$

- The convection heat transfer, $P_T$,

$$P_T = \int_S \left(hN_i F_\tau (T_\infty - T)\right)dS \tag{23}$$

- The curing capacity, $D_\alpha$,

$$D_\alpha = \int_L \int_A \left(N_i N_j F_\tau F_s\right)dA\,dL \tag{24}$$

- The cure kinetics function, $P_\alpha$,

$$P_\alpha = \int_L \int_A \left(N_i F_\tau f(\alpha,T)\right)dA\,dL \tag{25}$$

### 2.5. Newmark method

Eq. (19) can be rewritten in compact form,

$$\boldsymbol{C}\dot{\boldsymbol{q}} + \boldsymbol{K}\boldsymbol{q} = \boldsymbol{R} \tag{26}$$

$\boldsymbol{q}$ contains the temperature and degree of cure unknowns and $\boldsymbol{K}$ and $\boldsymbol{C}$ are the stiffness and damping matrices, respectively. $\boldsymbol{R}$ is the generalized force vector. This system is solved using the Newmark's method of integration (Bathe, 2006) and can be written at time step $t + \Delta t$ as:

$$\boldsymbol{C}\dot{\boldsymbol{q}}_{t+\Delta t} + \boldsymbol{K}\boldsymbol{q}_{t+\Delta t} = \boldsymbol{R}_{t+\Delta t} \tag{27}$$

The following equations are used for the vector of unknowns and its time derivative,

$$\begin{aligned} \dot{\boldsymbol{q}}_{t+\Delta t} &= \dot{\boldsymbol{q}}_t + [(1-\gamma)\ddot{\boldsymbol{q}}_t + \gamma\ddot{\boldsymbol{q}}_{t+\Delta t}]\Delta t \\ \boldsymbol{q}_{t+\Delta t} &= \boldsymbol{q}_t + \dot{\boldsymbol{q}}_t \Delta t + \left[\left(\frac{1}{2} - \beta\right)\ddot{\boldsymbol{q}}_t + \beta\ddot{\boldsymbol{q}}_{t+\Delta t}\right]\Delta t^2 \end{aligned} \tag{28}$$

$\gamma = 1/2$ and $\beta = 1/4$ are used. The solution for $\boldsymbol{q}_{t+\Delta t}$ is obtained by solving a linear system,

$$\hat{\boldsymbol{K}}\boldsymbol{q}_{t+\Delta t} = \hat{\boldsymbol{R}}_{t+\Delta t} \tag{29}$$

$\hat{\boldsymbol{K}}$ is the effective stiffness matrix,

$$\hat{\boldsymbol{K}} = \boldsymbol{K} + \frac{\gamma}{\beta\Delta t}\boldsymbol{C} \tag{30}$$

$\hat{\boldsymbol{R}}_{t+\Delta t}$ is the effective load vector,

$$\hat{\boldsymbol{R}}_{t+\Delta t} = \boldsymbol{R}_{t+\Delta t} + \boldsymbol{C}\left(\frac{\gamma}{\beta\Delta t}\boldsymbol{q}_t + \left(\frac{\gamma}{\beta} - 1\right)\dot{\boldsymbol{q}}_t + \frac{\Delta t}{2}\left(\frac{\gamma}{\beta} - 2\right)\ddot{\boldsymbol{q}}_t\right) \tag{31}$$

After finding the solution $\boldsymbol{q}_{t+\Delta t}$, $\dot{\boldsymbol{q}}_{t+\Delta t}$ and $\ddot{\boldsymbol{q}}_{t+\Delta t}$ can be updated:

$$\begin{aligned} \dot{\boldsymbol{q}}_{t+\Delta t} &= \dot{\boldsymbol{q}}_t + [(1-\gamma)\ddot{\boldsymbol{q}}_t + \gamma\ddot{\boldsymbol{q}}_{t+\Delta t}]\Delta t \\ \ddot{\boldsymbol{q}}_{t+\Delta t} &= \frac{1}{\beta\Delta t^2}(\boldsymbol{q}_{t+\Delta t} - \boldsymbol{q}_t) - \frac{1}{\beta\Delta t}\dot{\boldsymbol{q}}_t - \left(\frac{1}{2\beta} - 1\right)\ddot{\boldsymbol{q}}_t \end{aligned} \tag{32}$$

The Newmark method is unconditionally stable. Furthermore, in the present application, this scheme does not present stability problems, as the curing process exhibits relatively slow thermal and chemical dynamics. A fixed time interval is used during all simulations. The time interval size is selected based on a preliminary temporal convergence analysis. More details can be found in Bathe (2006).

## 3. Numerical results

This section aims to present and discuss numerical cases. First, the proposed approach is verified using cases from the literature. Then, the effect of various boundary conditions on temperature and cure distributions is evaluated. Finally, the curing process for a sandwich structure is analyzed.

### 3.1. Model verification

The model verification focuses on a plate made of 3501-6 epoxy and AS4 unidirectional carbon fibers (Bogetti, 1989). Table 1 gives the cure kinetics parameters related to this material. The plate is 2.54 cm thick, and the curing cycle has two holding temperatures, 116 °C for 70 min and 177 °C for 127 min. The heating rate is 2.24 °C/min and the cooling rate is 5 °C/min. The fiber volume fraction is 67%. The thermal properties of the composite part include the density, $\rho$ = 1520 kg/m$^3$, the specific heat $c$ = 942 J/(kg °C), and the thermal conductivity $k$ = 0.4457 W/(m °C). Convection is imposed on the top and bottom surfaces, the convection heat transfer coefficient is $h$ = 44.57 W/(m$^2$ K). As in Zappino et al. (2024b), the FE model has two B4 elements along the $y$-axis, see Fig. 2.

First, a convergence analysis of the structural theory was carried out to determine the number of Lagrange elements needed to obtain accurate results. Table 2 shows the temperature and degree of cure

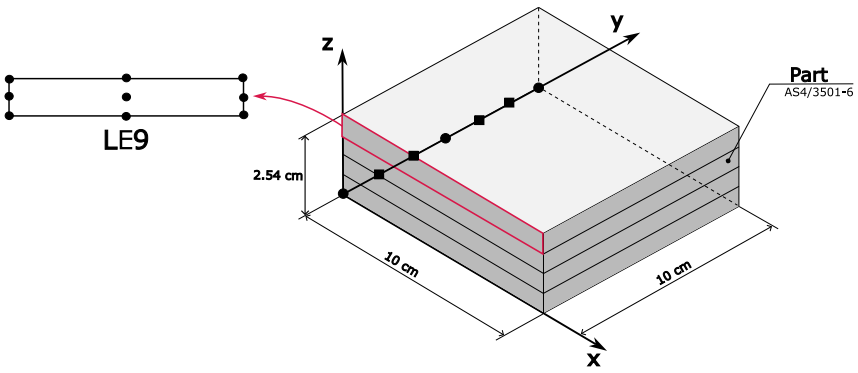



**Fig. 2.** Plate geometry and FE/CUF modeling.

**Table 2**
Temperature and degree of cure convergence increasing cross-section discretization; temperature and degree of cure evaluated at the center of the plate.

| Time | | 1 LE9 | 2 LE9 | 3 LE9 | 4 LE9 | 8 LE9 |
|---|---|---|---|---|---|---|
| 25 min | $T$ (°C) | 51.981 | 51.996 | 51.997 | 51.997 | 51.997 |
| | $\alpha$ [–] | 0.010 | 0.011 | 0.010 | 0.011 | 0.011 |
| 50 min | $T$ (°C) | 111.361 | 111.246 | 111.262 | 111.262 | 111.263 |
| | $\alpha$ [–] | 0.049 | 0.060 | 0.055 | 0.057 | 0.056 |
| 75 min | $T$ (°C) | 131.166 | 131.308 | 131.298 | 131.299 | 131.299 |
| | $\alpha$ [–] | 0.289 | 0.283 | 0.285 | 0.284 | 0.284 |
| 100 min | $T$ (°C) | 126.981 | 126.809 | 126.901 | 127.113 | 127.181 |
| | $\alpha$ [–] | 0.437 | 0.385 | 0.406 | 0.402 | 0.404 |
| 150 min | $T$ (°C) | 212.192 | 211.035 | 210.532 | 210.158 | 210.057 |
| | $\alpha$ [–] | 0.884 | 0.887 | 0.885 | 0.884 | 0.841 |
| 200 min | $T$ (°C) | 178.395 | 178.348 | 178.356 | 178.363 | 178.365 |
| | $\alpha$ [–] | 0.998 | 0.999 | 0.999 | 0.999 | 0.999 |
| DOF | | 126 | 210 | 294 | 378 | 714 |

at the center of the plate and at different curing times as the number of nine-point Lagrange elements (LE9) on the cross-section varies. Fig. 3 compares the temperature at the center of the composite plate for different cross-section models. Similarly, Fig. 4 shows the degree of cure during the curing process. The results show that convergence is achieved rapidly for temperature and degree of cure. Around the peak temperature, differences are more evident, and this suggests that 4 LE9 elements in the cross-section provide the highest accuracy. Instead, the degree of cure variation is more evident in the final part of the first holding temperature. In this case, 3 LE9 is enough. The selected model for the following simulations is 4 LE9 as shown in Fig. 2. The second convergence analysis considered the number of Newmark steps. Table 3 shows the temperature and degree of cure as time steps increase. The degree of cure does not change significantly; on the contrary, the temperature shows a more significant dependence on the number of iterations. Fig. 5 shows the temperature evolution at the central point of the structure during the curing process with a different number of iterations. Differences are more evident at the first peak, and 1500 iterations will be used for all following cases. Using the selected model, the total runtime for this simulation is 43.67 s, 13th Gen Intel(R) Core(TM) i7-13620H (2.40 GHz), RAM 16.0 GB. After the convergence study, the accuracy of the model was verified by comparing it with the results by Bogetti (1989), obtained through a 1D model, see Fig. 6. A perfect match was found, verifying the accuracy of the proposed approach.

A second verification was carried out on a similar plate of 3501-6 epoxy and AS4 unidirectional carbon fibers and 2.54 cm thick as in Ren et al. (2018). A new set of boundary conditions is considered. Instead of convection along the $z$-direction, a temperature equal to that of the autoclave is imposed at the top and bottom surfaces. The specific heat is $c$ = 862 J/(kg °C), the density is $\rho$ = 1578 kg/m$^3$ and the thermal conductivity is $k$ = 0.4135 W/(m °C). Table 1 provides the cure kinetics parameters. The curing process consists of a first holding temperature at 116 °C for 60 min and a second one at 177 °C for 120 min. The heating rates are 2.43 °C/min and 3 °C/min. Fig. 7 shows comparisons with the results at the center point of the structure from Ren et al. (2018), where 3D, 1D, and experimental results are shown. The results suggest that

- Parabolic LW cross-sectional models effectively detect the cure and temperature distributions. Four LW elements ensure converged results.
- The temperature distribution is more affected by the discretization and time steps than the curing rate. The regions around the temperature peaks are those requiring more refined models.
- The present approach matches results from 3D models and experiments almost perfectly.

### 3.2. Spatially varying convective boundary conditions

This section focuses on spatially variable convective boundary conditions over the laminate surface. The purpose of this case is not to reproduce a specific autoclave configuration in a completely realistic way, but rather to demonstrate that the proposed 3D thermochemical model can adapt to non-homogeneous heat transfer conditions and quantify their influence on the predicted temperature field and the distribution of the degree of cure. During autoclave processing, spatial variations in the convective heat transfer coefficient may occur due to the position of parts within the autoclave, shielding effects caused by tools and adjacent parts, and non-uniform airflow patterns induced by the internal circulation system (Fisher et al., 2023; Fernlund et al., 2018). The present, simplified configuration provides a controlled benchmark for evaluating the sensitivity of cure predictions to such non-uniform boundary conditions and can be extended in future work to more realistic autoclave loading configurations.

The numerical case considers a 1.22 cm thick composite laminate composed of 8552 epoxy resin reinforced with AS4 carbon fibers (Johnston, 1997). The fiber volume fraction is 57.3% and the cure kinetics is modeled using Eq. (6). The composite comprises eight layers of equal thickness, with $[90/0/90/0]_s$ stacking sequence. The orientation angle is defined with respect to the $z$-axis, with the fibers at 0° aligned to the $x$-axis, while the fibers at 90° aligned to the $y$-axis. The density $\rho$ = 1580 kg/m$^3$; the specific heat is $c$ = 1281 J/(kg °C); the thermal conductivity components are $k_1$ = 6.104 W/(m °C) and $k_2$ = $k_3$ = 2.004 W/(m °C). The plate is on an Invar tool 1.27 cm thick, with a density of 8140 kg/m$^3$, specific heat of 515 J/(kg °C), and the thermal conductivity coefficient is $k$ = 10.7 W/(m °C). The curing cycle consists

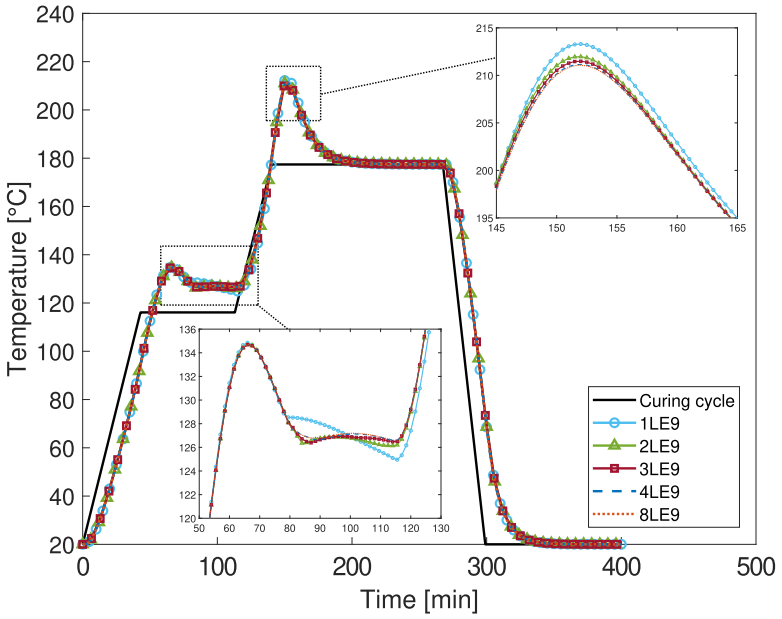



**Fig. 3.** Comparison of the temperature during the curing process for different cross-section discretizations.

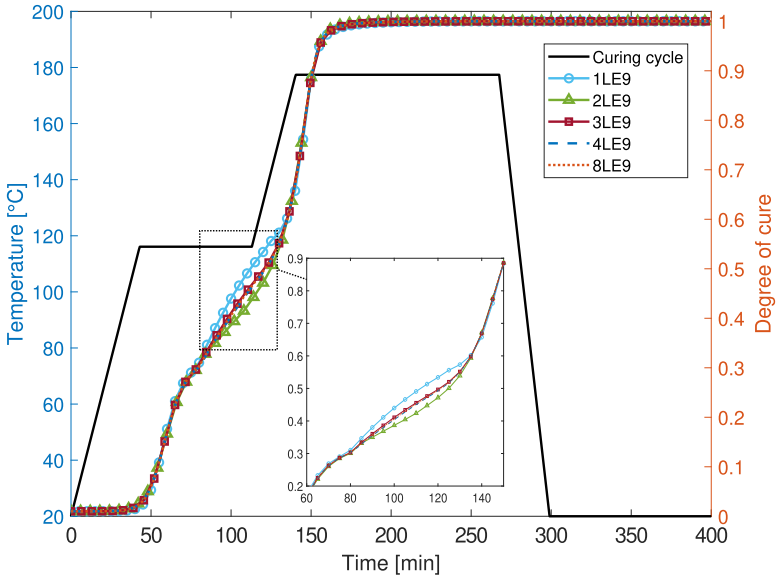



**Fig. 4.** Comparison of the degree of cure during the curing process for different cross-section discretizations.

**Table 3**
Temperature and degree of cure convergence increasing time steps; temperature and degree of cure evaluated at the center of the plate.

| Time | | 600 | 700 | 800 | 900 | 1100 | 1500 | 2000 |
|---|---|---|---|---|---|---|---|---|
| 20 min | T (°C) | 42.953 | 42.997 | 43.029 | 43.054 | 43.091 | 43.134 | 43.164 |
| | $\alpha$ [–] | 0.010 | 0.010 | 0.010 | 0.010 | 0.010 | 0.010 | 0.010 |
| 40 min | T (°C) | 86.617 | 86.651 | 86.676 | 86.696 | 86.725 | 86.760 | 86.785 |
| | $\alpha$ [–] | 0.019 | 0.019 | 0.019 | 0.019 | 0.019 | 0.020 | 0.020 |
| 80 min | T (°C) | 128.247 | 127.936 | 127.871 | 127.741 | 127.676 | 127.602 | 127.552 |
| | $\alpha$ [–] | 0.308 | 0.304 | 0.303 | 0.301 | 0.299 | 0.298 | 0.297 |
| 160 min | T (°C) | 202.535 | 202.907 | 201.661 | 202.058 | 201.542 | 201.316 | 201.099 |
| | $\alpha$ [–] | 0.976 | 0.973 | 0.976 | 0.974 | 0.975 | 0.974 | 0.974 |

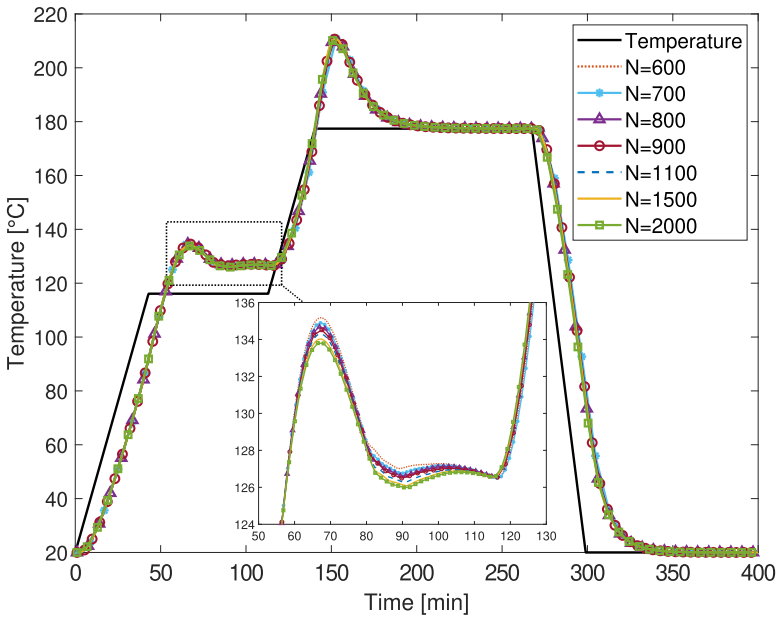



**Fig. 5.** Comparison of the temperature during the curing process for different time steps.

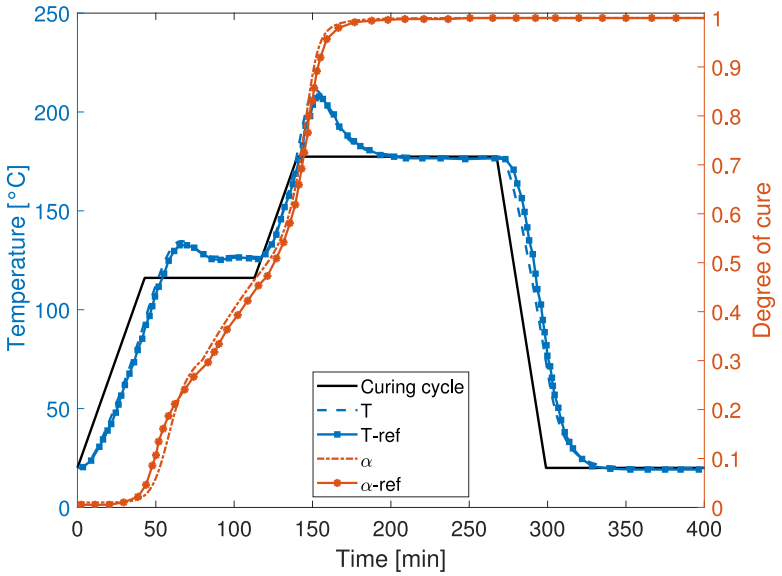



**Fig. 6.** Comparison of temperature and degree of cure during the curing process with reference results (Bogetti, 1989).

of a heating phase at 1.8 °C/min up to a holding temperature of 177 °C, maintained for 200 min, followed by a cooling phase at 4 °C/min. The tool and the composite plate structure are subjected to convection on all the external surfaces with a convection heat transfer coefficient equal to $h = 60$ W/(m$^2$ K). The only area heated with a lower $h$ is a central square area on the top surface of size 0.033 m × 0.033 m, in which the convection heat transfer coefficient is $h = 40$ W/(m$^2$ K). Each layer and the tool have three LE9, while three B4 were used along the beam axis, as shown in Fig. 8, with 2660 DOF. Fig. 9 compares the temperature profiles at two points – P1 and P2, see Fig. 8 – highlighting the peak area where the differences between the profiles are more evident. Table 4 presents the temperature and degree of cure at different locations along the $y$-direction and at various times. Fig. 10 shows the temperature along the $y$-directions at $t = 75$ min and $x = 0.05$ m; two pints along the thickness were considered. The current non-homogeneous case is compared with a homogeneous one with $h = 60$ W/(m$^2$ K). Two examples of 3D temperature distribution in the composite part at $t = 50$ min and $t = 100$ min are shown in Fig. 11. For the same time instants, Fig. 12 shows the corresponding cross-sectional view, to visualize the temperature gradients across the thickness. For completeness, Appendix A shows the temperature and degree of cure trends along the thickness for P1 and P2 at various points in the curing cycle.

The results show that

- Temperature and degree of cure vary along the three spatial directions. The magnitude of in-plane variations are similar, while, along the thickness, the temperature variation is more significant than the degree of cure.
- The localized reduction in heat transfer coefficient affects temperature gradients and values.
- Over time, the spatial variation of the degree of cure tends to decrease; the temperature variations are not affected by the curing time.

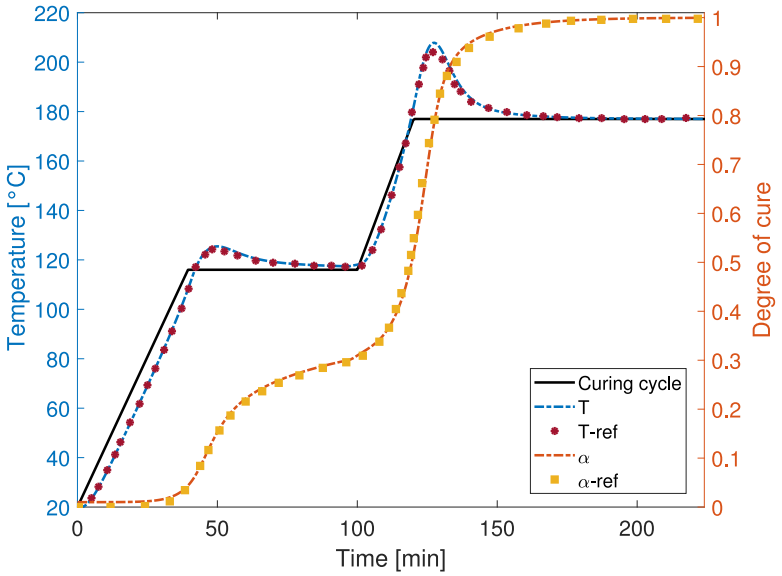



**Fig. 7.** Comparison of temperature and degree of cure during the curing process with reference results with temperature boundary conditions (Ren et al., 2018).

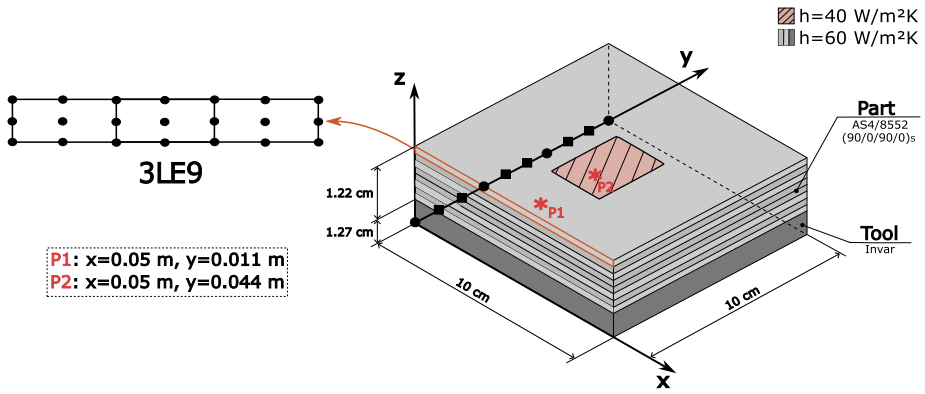



**Fig. 8.** Geometry and discretization of the plate under non-homogeneous convection.

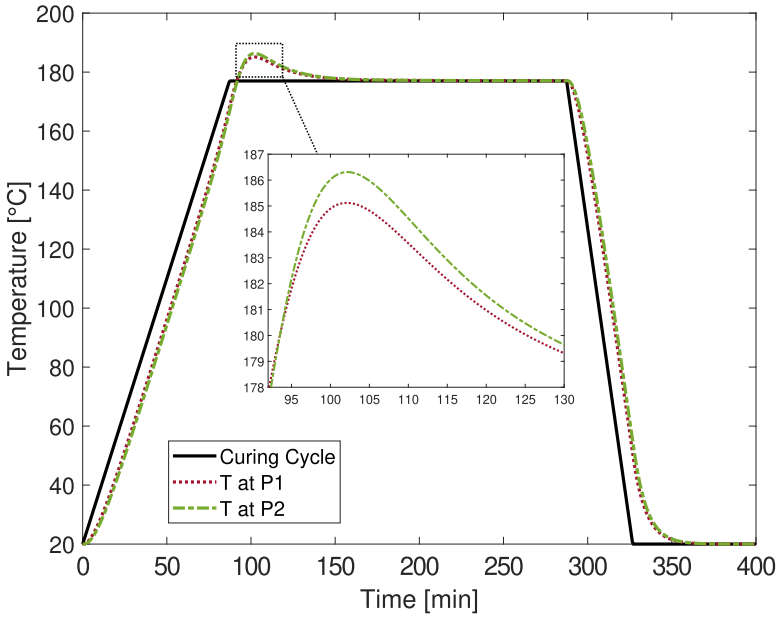



**Fig. 9.** Comparison of the temperature in two different points in the case of non-homogeneous heating, $z = 1.88$ cm.

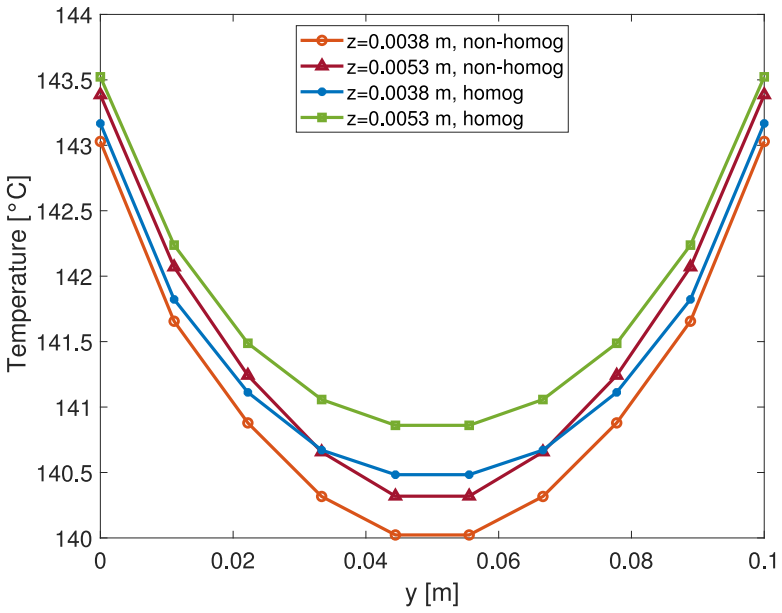


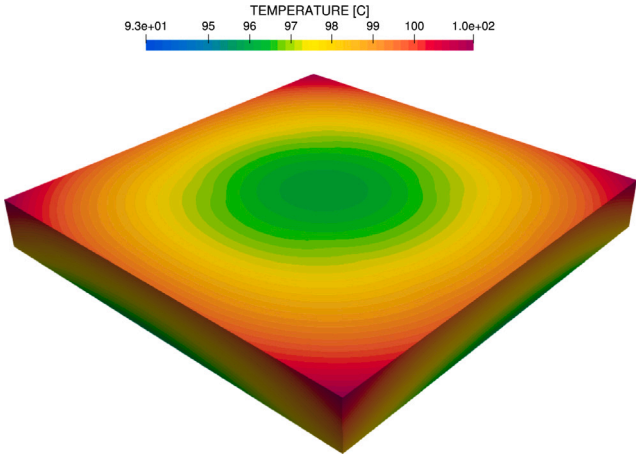

**Fig. 10.** Comparison of temperature along the $y$-axis at $t$ = 75 min and $x$ = 0.05 m, non-homogeneous and homogeneous heating cases.

**Table 4**
Temperature and degree of cure at different y locations and times, x = 0.05 m and z = 0.0061 m, non-homogeneous heating case.

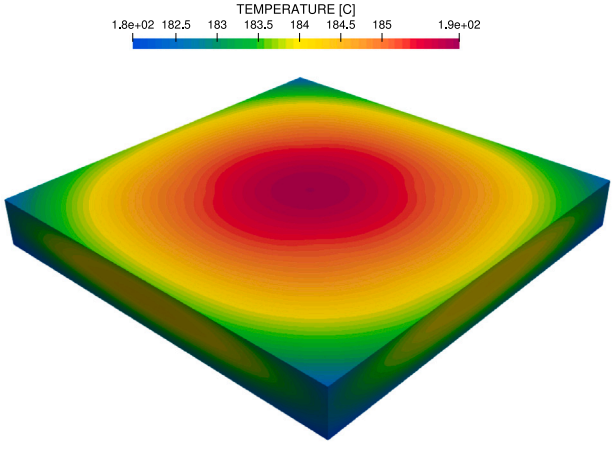
| Time | | 0 m | 0.011 m | 0.022 m | 0.033 m | 0.044 m |
|---|---|---|---|---|---|---|
| 25 min | $T$ (°C) | 52.776 | 51.423 | 50.538 | 49.897 | 49.501 |
| | $\alpha$ [–] | 0.050 | 0.050 | 0.050 | 0.050 | 0.050 |
| 80 min | $T$ (°C) | 153.254 | 151.977 | 151.111 | 150.455 | 150.061 |
| | $\alpha$ [–] | 0.128 | 0.108 | 0.111 | 0.102 | 0.103 |
| 100 min | $T$ (°C) | 184.103 | 184.910 | 185.434 | 185.866 | 186.135 |
| | $\alpha$ [–] | 0.502 | 0.495 | 0.493 | 0.487 | 0.486 |
| 300 min | $T$ (°C) | 149.671 | 152.112 | 153.661 | 154.767 | 155.450 |
| | $\alpha$ [–] | 0.831 | 0.831 | 0.831 | 0.831 | 0.832 |

### 3.3. Sandwich structure

This section focuses on a hybrid solid laminate/honeycomb structure, as described in Johnston (1997). This structure was developed within the ATCAS project (Ilcewicz et al., 1997), aimed at optimizing the process in terms of cost and weight by employing complex structures as sandwiches. The sandwich structure in this work consists of a solid composite section, a honeycomb section, and a transition zone between the two in which the core thickness gradually decreases. The geometry of the composite part is shown in Fig. 13. The composite material is the unidirectional AS4/8552 prepreg, while the honeycomb core material is HEXCEL glass phenolic HRP-3/16-8.0. The properties of these materials are given in Tables 5 and 6. In Johnston (1997), the composite properties are considered non-constant during the process and are temperature dependent. In the model proposed in this paper, thermophysical properties are kept constant and are calculated using the formulas in Johnston (1997) in three different cases, at the minimum temperature ($T$ = 20 °C), at an intermediate temperature ($T$ = 149 °C), and at the maximum temperature ($T$ = 177 °C) of the curing process, as shown in Table 5, more details on the effect of such parameters on the results follow. The fiber volume fraction of the AS4/8552 composite is $V_f$ = 0.573. The cure kinetics is modeled using Eq. (6) as in the reference. The curing cycle consists of three stages: a first holding temperature of 107 °C for 200 min, a second holding temperature of 149 °C for 90 min, and a third holding temperature of

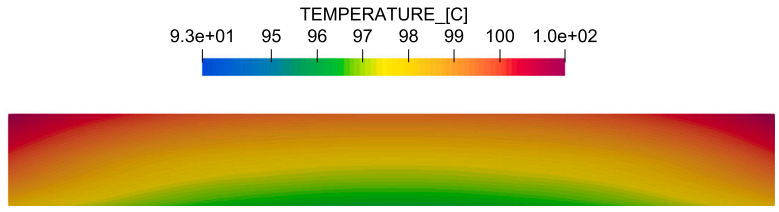



(a) $t$ = 50 min.

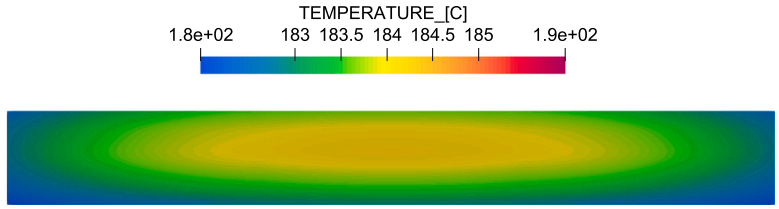



(b) $t$ = 100 min.

**Fig. 11.** 3D temperature distribution, non-homogeneous case.




(a) $t$ = 50 min.




(b) $t$ = 100 min.

**Fig. 12.** Temperature distributions along the thickness, non-homogeneous case.

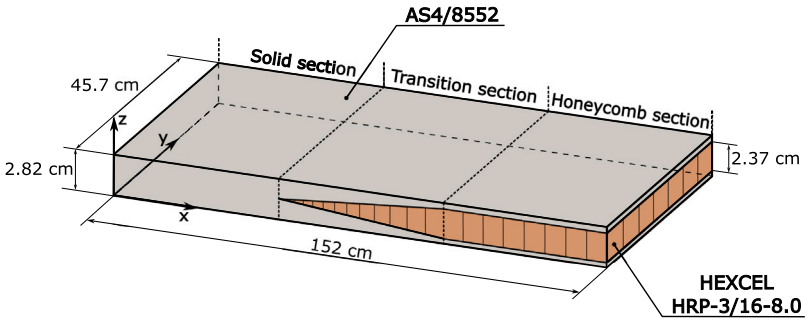



**Fig. 13.** Sandwich structure geometry.

**Table 5**
Thermophysical properties of the AS4/8552.

| AS4/8552 | | | |
|---|---|---|---|
| | props @ 20 °C | props @ 149 °C | props @ 177 °C |
| Density (kg/m$^3$) | $\rho$ = 1580 | $\rho$ = 1580 | $\rho$ = 1580 |
| Specific heat capacity (J/(kg K)) | $c_p$ = 866.31 | $c_p$ = 1207.31 | $c_p$ = 1281.33 |
| Thermal conductivity (W/(m K)) | $k_l$ = 4.677<br>$k_t$ = 0.455 | $k_l$ = 5.849<br>$k_t$ = 0.709 | $k_l$ = 6.104<br>$k_t$ = 0.740 |

**Table 6**
Thermophysical properties of the HEXCEL HRP-3/16-8.0.

| HEXCEL HRP-3/16-8.0 | |
|---|---|
| Density (kg/m$^3$) | $\rho$ = 128 |
| Specific heat capacity (J/(kg K)) | $c_p$ = 1260 |
| Thermal conductivity (W/(m K)) | $k$ = 0.0706+3.4 × 10$^{-4}$ |

177 °C for 145 min. The heating rate is 1.1 °C/min while the cooling rate is 2.5 °C/min.

As shown in Fig. 14, a reinforced rubber caul 4.8 mm thick is placed on the top surface. This plate is used during the process to allow a homogeneous pressure application. The density of the caul is 1400 kg/m$^3$ and the conductivity 0.68 W/(m K). In this case, the specific heat capacity also depends on the temperature of the curing cycle. The minimum value used is $c_p$ = 1124 J/(kg K), the intermediate value is $c_p$ = 1536.8 J/(kg K), and the maximum value is $c_p$ = 1626.4 J/(kg K). The sandwich structure is placed on an Invar tool 2.5 cm thick. The thermophysical properties of this material are the following: $\rho$ = 8140 kg/m$^3$, $c_p$ = 515 J/(kg K), $k$ = 10.7 W/(m K). Convection is applied to the top and bottom surfaces. The heat transfer coefficients are $h$ = 21.899 W/(m$^2$ K) at the top and $h$ = 58.831 W/(m$^2$ K) at the bottom. The FE model along the $y$-axis consists of two B4 elements. The part, caul plate, and tool cross-sections are discretized using 18 LE9, as shown in Fig. 14. The number of DOF is 1274. The analysis was performed using 700 time steps ($\Delta t$ = 1 min), resulting in a total runtime of 167.01 s. The adopted time discretization was selected after a convergence study on the temperature and degree of cure fields. The nodes shown in red in Fig. 14 are the points where the results are evaluated. Specifically, points 1, 2, and 3 are along the thickness of the solid section, while nodes 4 and 5 are in the middle of the composite skins in the honeycomb section. These positions were selected accordingly to those adopted in the reference study. Appendix B reports the full set properties over the curing cycle.

Fig. 15 compares the temperature and degree of cure results at the center of the solid section, considering the composite properties calculated at 20 °C, 149 °C, and 177 °C, while the reference solution is from Johnston (1997). Similarly, Fig. 16 shows the temperature and degree of cure at point 5 (see Fig. 14) in the honeycomb section. The results show that the curves differ from the reference values

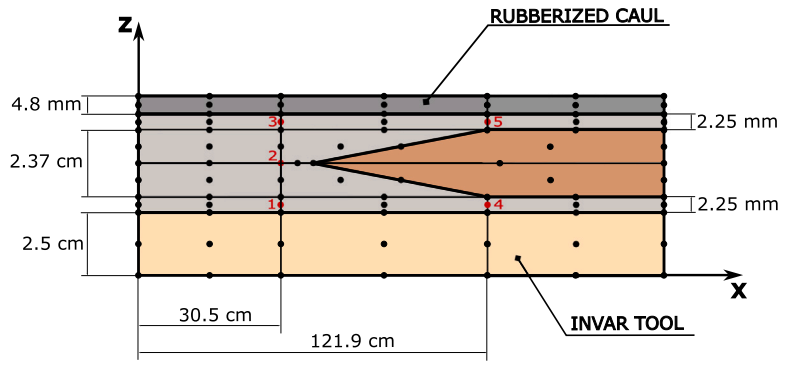



**Fig. 14.** Geometry and discretization of the cross-sections of the sandwich, tool, and caul plate.

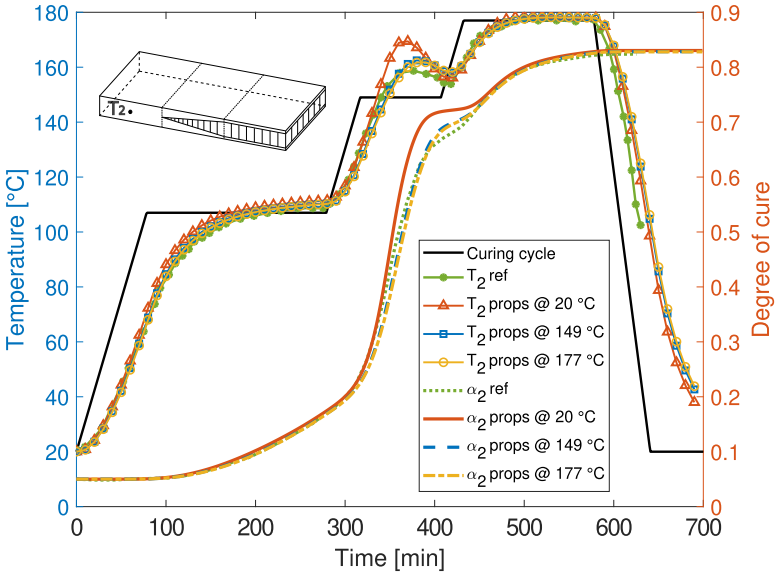



**Fig. 15.** Comparison of temperature and degree of cure at solid section point 2 in the sandwich structure, obtained using minimum, intermediate, and maximum composite properties with reference results (Johnston, 1997).

when considering the minimum properties. However, when using the intermediate and maximum properties, the temperature and degree of cure trends are close to the reference. In the solid section, the differences are greater than in the honeycomb section. In fact, in the latter case, the composite properties have a very low impact on the results, since the two composite skins are much thinner than the core. These findings also support the modeling assumption adopted in this work that constant thermal properties are used. The objective of the proposed thermochemical formulation is to integrate it with a mechanical model to predict process-induced residual deformations, which predominantly develop after the gelation point. In the post-gelation regime, material properties can be reasonably approximated by their values at elevated temperatures. Accordingly, the maximum thermal properties are employed in the subsequent analyses, as they yield results closer to the reference solution.

Fig. 17 shows the temperature and degree of cure at points 1, 2, and 3 along the thickness of the solid section, while Fig. 18 shows the temperature and degree of cure at points 4 and 5 of the honeycomb section. The differences between the two sections are significant. In particular, at the second holding temperature, the exothermic chemical reactions in the composite resin cause the temperature to peak in the solid section, but not in the honeycomb section. This behavior is mainly associated with the reduction in the thickness of the composite skins in the honeycomb section, which limits the total amount of resin available for polymerization. As a result, the exothermic heat generated within the skins is insufficient to raise the autoclave temperature. Furthermore, it can be observed that the points within the honeycomb section heat up more rapidly than the corresponding points in the solid section, particularly during the initial heating stage of the curing cycle. This effect is related to the lower thermal inertia of the sandwich configuration. Tables 7 and 8 show the temperature and degree of cure along the thickness of the solid and the honeycomb sections for different time instants of the curing process. In the honeycomb section, the Hexcel glass/phenolic core exhibits a significantly lower through-thickness thermal conductivity than the epoxy-based composite skins. This pronounced anisotropy strongly inhibits heat diffusion across the core, leading to strong temperature gradients and, consequently, to significant variations in the degree of cure. The tool also prevents the bottom surface of the sandwich from heating as fast as the top surface. Figs. 19(a) and 19(b) show temperature distributions along the thickness in the sandwich structure at $t$ = 150 min and $t$ = 400 min, respectively. The 3D distributions of temperature and degree of cure at $t$ = 400 min are shown in Fig. 20. Finally, Fig. 21 shows the temperature and degree of cure along the thickness of the honeycomb section at different points and times. By comparing three time instances, it is evident that through-thickness gradients develop in both temperature and degree of cure, due to the presence of the honeycomb core.

The results show that

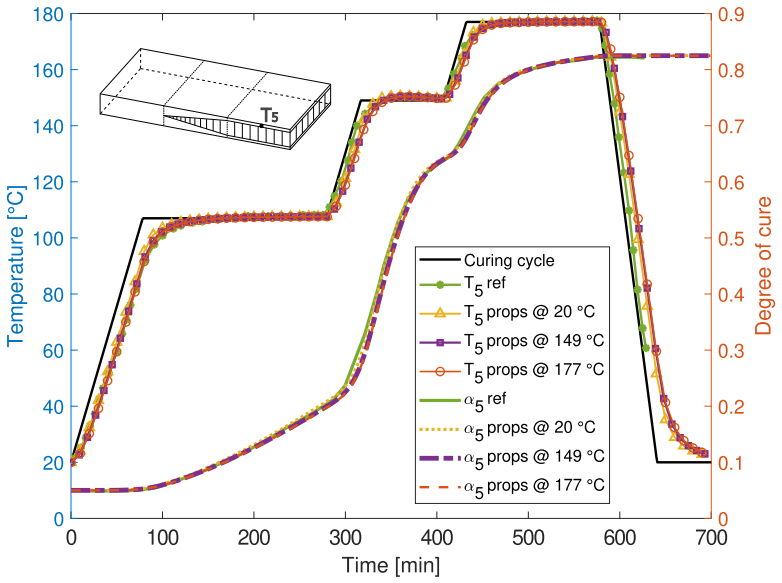



**Fig. 16.** Comparison of temperature and degree of cure at honeycomb section point 5 in the sandwich structure, obtained using minimum, intermediate, and maximum composite properties, with reference results (Johnston, 1997).

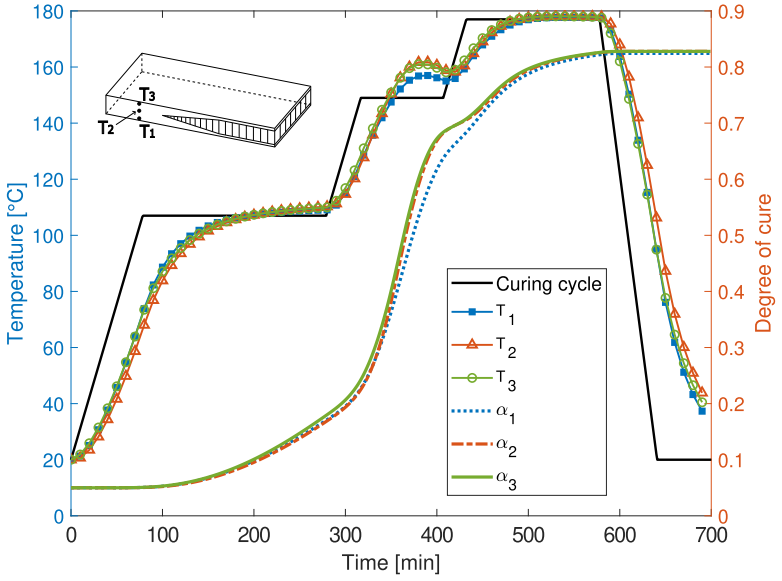



**Fig. 17.** Temperature and degree of cure at points 1, 2, and 3 of the solid section of the sandwich structure.

**Table 7**
Temperature and degree of cure at different z locations in the solid section and times, x = 15.25 m and y = 0.0 m.

| Time | | 25 mm | 26.125 mm | 27.25 mm | 39.1 mm | 50.95 mm | 52.075 mm | 53.2 mm |
|---|---|---|---|---|---|---|---|---|
| 300 min | $T$ [°C] | 114.331 | 114.298 | 114.277 | 114.678 | 116.354 | 116.586 | 116.830 |
| | $\alpha$ [–] | 0.195 | 0.195 | 0.193 | 0.193 | 0.198 | 0.207 | 0.203 |
| 350 min | $T$ [°C] | 144.247 | 144.939 | 145.661 | 150.421 | 151.205 | 151.096 | 150.951 |
| | $\alpha$ [–] | 0.363 | 0.363 | 0.364 | 0.382 | 0.398 | 0.401 | 0.403 |
| 400 min | $T$ [°C] | 156.116 | 156.676 | 157.249 | 160.642 | 160.190 | 159.970 | 159.721 |
| | $\alpha$ [–] | 0.617 | 0.624 | 0.630 | 0.669 | 0.673 | 0.672 | 0.671 |

- The 1D modeling approach proposed in this paper effectively predicts temperature and degree of cure distributions.
- The variation in the thermophysical properties of the composite has a greater impact on the solid section than on the honeycomb section in terms of temperature and degree of cure. The use of maximum properties best reflects the reference results.
- The gradients of temperature and degree of cure along the thickness are much higher in the honeycomb section than in the solid section since the core has lower conductivity than the composite.
- The amount of exothermic reactions is higher in the solid section, resulting in a temperature peak at the second holding temperature.

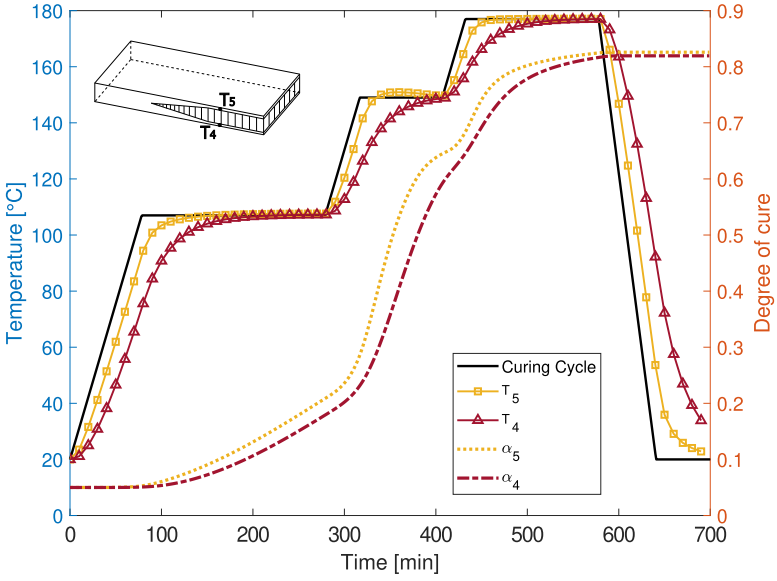
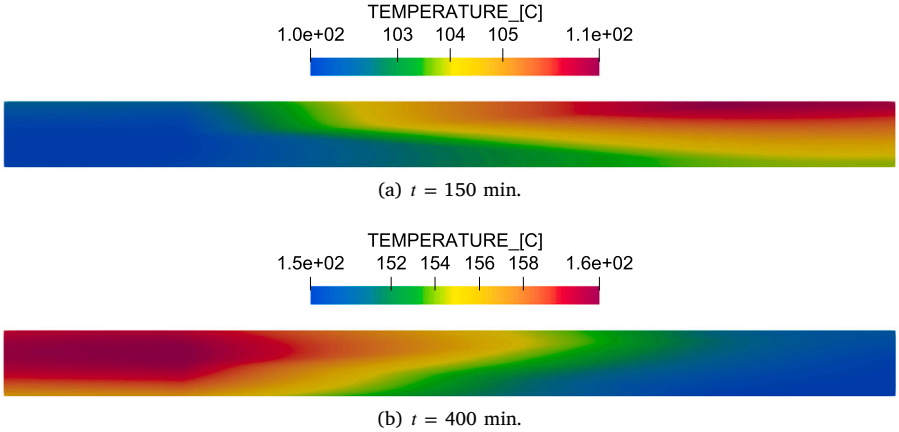



**Fig. 18.** Temperature and degree of cure at points 4 and 5 of the honeycomb section of the sandwich structure.

**Table 8**
Temperature and degree of cure at different z locations in the honeycomb section and times, x = 152 m and y = 0.0 m.

| Time | | 25 mm | 26.125 mm | 27.25 mm | 39.1 mm | 50.95 mm | 52.075 mm | 53.2 mm |
|---|---|---|---|---|---|---|---|---|
| 300 min | $T$ [°C] | 113.134 | 113.104 | 113.089 | 114.055 | 118.784 | 118.859 | 118.964 |
| | $\alpha$ [−] | 0.202 | 0.189 | 0.231 | [a] | 0.259 | 0.223 | 0.241 |
| 350 min | $T$ [°C] | 141.300 | 141.363 | 141.394 | 143.757 | 149.823 | 149.856 | 149.840 |
| | $\alpha$ [−] | 0.360 | 0.351 | 0.374 | [a] | 0.454 | 0.464 | 0.464 |
| 400 min | $T$ [°C] | 148.383 | 148.436 | 148.463 | 148.487 | 149.764 | 149.764 | 149.751 |
| | $\alpha$ [−] | 0.572 | 0.573 | 0.573 | [a] | 0.632 | 0.631 | 0.633 |

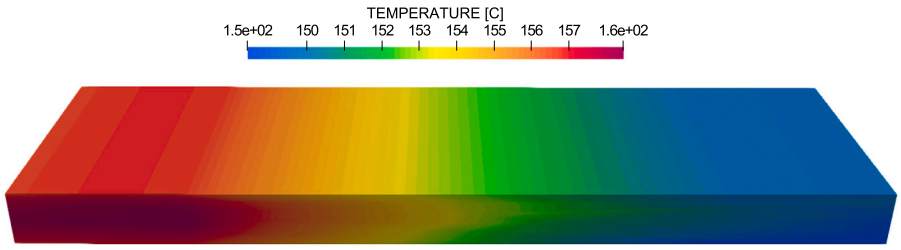
[a] Position in the thickness corresponding to the core, where no degree of cure value is defined.



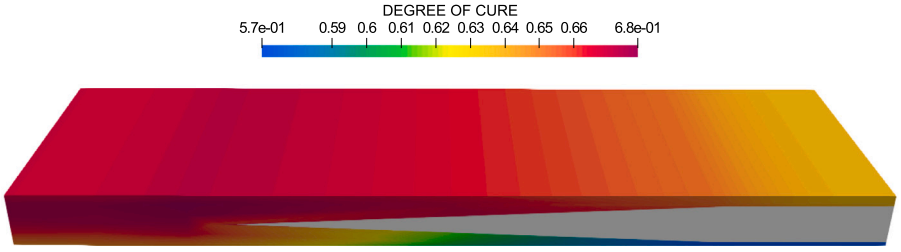

(a) $t$ = 150 min.

(b) $t$ = 400 min.

**Fig. 19.** Temperature distributions along the thickness, sandwich case.




(a) Temperature.




(b) Degree of cure.

**Fig. 20.** 3D distribution of temperature and degree of cure at t = 400 min, sandwich case.

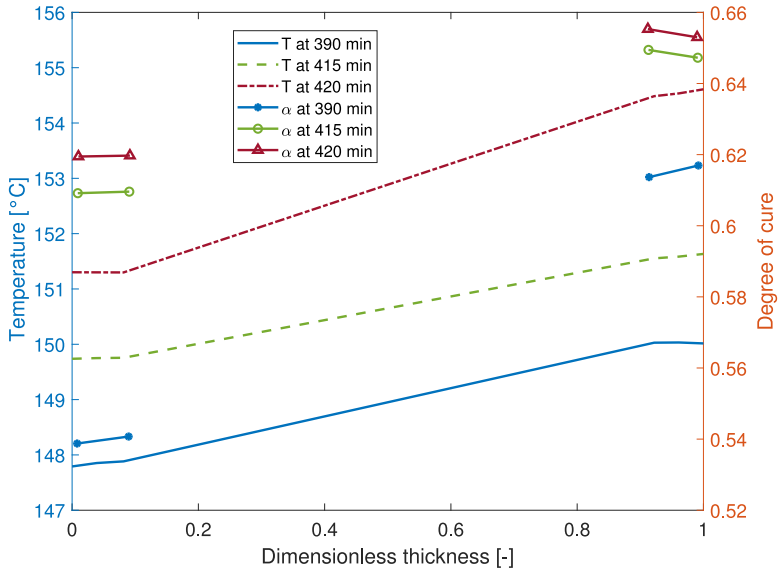



**Fig. 21.** Temperature and degree of cure along the thickness in the honeycomb section for different time instants, sandwich case.

## 4. Conclusion

This paper presents numerical simulations of the curing process for composite plates and sandwich structures under temperature and convection boundary conditions. The numerical model has two primary variables: the temperature and the degree of cure. The model employs 1D finite elements, while, along the cross-section, higher-order distributions of temperature and degree of cure are used using the Carrera Unified Formulation. A layer-wise approach was used, in which each layer was explicitly modeled with a set of unknown variables. Boundary conditions included the imposition of temperature, convection, and homogeneous and non-homogeneous distributions. The model was verified using results from the literature. The results considered the 3D temperature distribution and degree of cure over time. The following conclusion can be drawn:

- The CUF-based methodology developed in this work enables the prediction of temporal and 3D spatial temperature distributions and degree of cure with low runtimes. Although the formulation is 1D, 3D fields can be obtained; moreover, the present model captures the effects of non-uniform thermal boundary conditions
- The model was verified against literature-reported reference results for both the composite plate and the sandwich configuration, showing a close match in temperature and degree of cure.
- In the sandwich structure, the results showed that the presence of a core of a different material significantly influences the temperature and degree of cure along the thickness. In regions with the core, thin composite skins have fewer chemical reactions, whereas in fully composite sections, temperatures increase significantly.
- The lower thermal conductivity of the sandwich structure core results in increased temperature and degree of cure gradients along the thickness compared to the fully composite section.

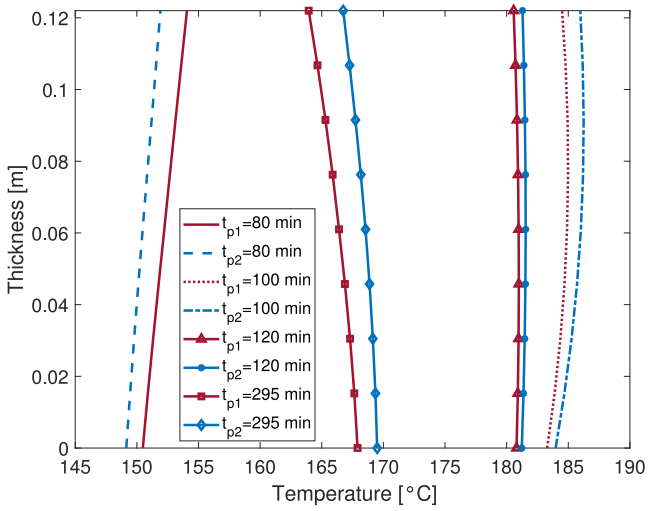
Future developments aim to couple the present thermochemical model with the mechanical one. The focus is on analyzing the effect of

**Table 9**
Evolution of material properties during the curing process at point 2 of the sandwich structure.

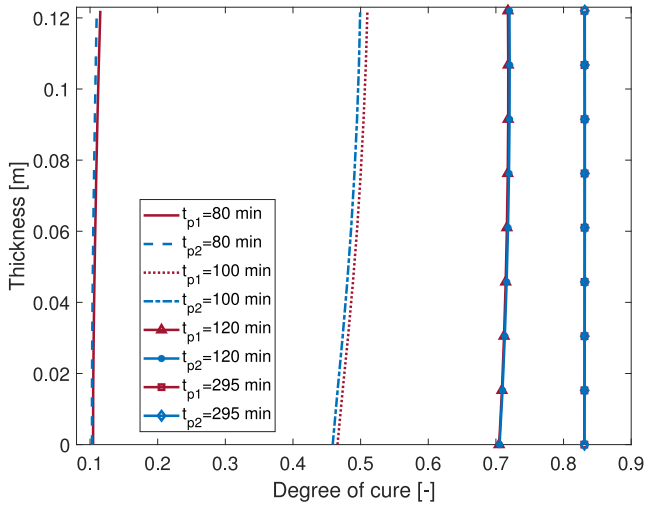
| $t$ [s] | $T$ [°C] | $\alpha$ [–] | $E_L$ [GPa] | $E_Z, E_X$ [MPa] | $\nu_{LX,LZ}$ [–] | $\nu_{XZ}$ [–] | $G_{LX,LZ}$ [MPa] | $G_{XZ}$ [MPa] |
|---|---|---|---|---|---|---|---|---|
| 370 | 160.02 | 0.529 | 118.72 | 1905.77 | 0.249 | 0.319 | 939.92 | 722.68 |
| 380 | 161.70 | 0.590 | 118.95 | 3584.39 | 0.250 | 0.329 | 1837.70 | 1349.05 |
| 390 | 161.76 | 0.637 | 119.13 | 4723.91 | 0.250 | 0.335 | 2487.65 | 1769.13 |
| 400 | 160.64 | 0.669 | 119.25 | 5438.96 | 0.250 | 0.339 | 2913.22 | 2030.72 |
| 410 | 158.80 | 0.686 | 119.32 | 5821.38 | 0.250 | 0.341 | 3146.63 | 2170.01 |
| 420 | 158.25 | 0.696 | 119.35 | 6021.38 | 0.250 | 0.342 | 3270.34 | 2242.70 |
| 430 | 160.47 | 0.704 | 119.38 | 6182.88 | 0.250 | 0.343 | 3371.07 | 2301.31 |
| 440 | 164.84 | 0.714 | 119.42 | 6392.40 | 0.251 | 0.345 | 3502.87 | 2377.23 |
| 450 | 169.04 | 0.729 | 119.48 | 6679.01 | 0.251 | 0.346 | 3685.22 | 2480.90 |
| 460 | 172.30 | 0.745 | 119.54 | 6995.08 | 0.251 | 0.348 | 3889.12 | 2594.97 |
| 470 | 174.59 | 0.761 | 119.60 | 7287.60 | 0.251 | 0.349 | 4080.46 | 2700.30 |
| 480 | 176.09 | 0.775 | 119.65 | 7531.85 | 0.251 | 0.351 | 4242.19 | 2788.08 |
| 490 | 177.03 | 0.786 | 119.69 | 7726.23 | 0.251 | 0.352 | 4372.19 | 2857.83 |
| 500 | 177.60 | 0.794 | 119.72 | 7878.86 | 0.251 | 0.353 | 4475.08 | 2912.53 |
| 510 | 177.92 | 0.801 | 119.75 | 7999.30 | 0.251 | 0.353 | 4556.77 | 2955.66 |
| 520 | 178.09 | 0.807 | 119.77 | 8095.54 | 0.251 | 0.354 | 4622.37 | 2990.10 |
| 530 | 178.15 | 0.812 | 119.79 | 8173.66 | 0.251 | 0.354 | 4675.82 | 3018.03 |
| 540 | 178.16 | 0.815 | 119.80 | 8238.08 | 0.251 | 0.355 | 4720.05 | 3041.05 |
| 550 | 178.12 | 0.819 | 119.81 | 8292.08 | 0.251 | 0.355 | 4757.22 | 3060.35 |
| 560 | 178.06 | 0.821 | 119.82 | 8338.01 | 0.251 | 0.355 | 4788.90 | 3076.75 |
| 570 | 177.99 | 0.824 | 119.83 | 8377.65 | 0.251 | 0.355 | 4816.30 | 3090.90 |
| 580 | 177.90 | 0.826 | 119.84 | 8412.29 | 0.251 | 0.355 | 4840.28 | 3103.27 |
| 590 | 175.42 | 0.827 | 119.84 | 8438.12 | 0.251 | 0.356 | 4858.19 | 3112.49 |
| 600 | 167.94 | 0.828 | 119.85 | 8446.41 | 0.251 | 0.356 | 4863.94 | 3115.44 |
| 610 | 156.48 | 0.828 | 119.85 | 8447.27 | 0.251 | 0.356 | 4864.54 | 3115.75 |
| 620 | 141.94 | 0.828 | 119.85 | 8447.30 | 0.251 | 0.356 | 4864.56 | 3115.76 |
| 630 | 125.01 | 0.828 | 119.85 | 8447.30 | 0.251 | 0.356 | 4864.56 | 3115.76 |
| 640 | 106.24 | 0.828 | 119.85 | 8447.30 | 0.251 | 0.356 | 4864.56 | 3115.76 |
| 650 | 87.25 | 0.828 | 119.85 | 8447.30 | 0.251 | 0.356 | 4864.56 | 3115.76 |
| 660 | 71.93 | 0.828 | 119.85 | 8447.30 | 0.251 | 0.356 | 4864.56 | 3115.76 |
| 670 | 60.06 | 0.828 | 119.85 | 8447.30 | 0.251 | 0.356 | 4864.56 | 3115.76 |
| 680 | 50.91 | 0.828 | 119.85 | 8447.30 | 0.251 | 0.356 | 4864.56 | 3115.76 |
| 690 | 43.85 | 0.828 | 119.85 | 8447.30 | 0.251 | 0.356 | 4864.56 | 3115.76 |
| 700 | 38.89 | 0.828 | 119.85 | 8447.30 | 0.251 | 0.356 | 4864.56 | 3115.76 |

**Table 10**
Evolution of material properties during the curing process at point 5 of the sandwich structure.

| $t$ [s] | $T$ [°C] | $\alpha$ [–] | $E_L$ [GPa] | $E_Z, E_X$ [MPa] | $\nu_{LX,LZ}$ [–] | $\nu_{XZ}$ [–] | $G_{LX,LZ}$ [MPa] | $G_{XZ}$ [MPa] |
|---|---|---|---|---|---|---|---|---|
| 370 | 150.42 | 0.559 | 118.84 | 2770.51 | 0.249 | 0.324 | 1393.83 | 1046.51 |
| 380 | 150.28 | 0.592 | 118.96 | 3650.88 | 0.250 | 0.329 | 1874.70 | 1373.67 |
| 390 | 150.03 | 0.616 | 119.05 | 4232.98 | 0.250 | 0.332 | 2203.46 | 1588.64 |
| 400 | 149.76 | 0.631 | 119.11 | 4601.70 | 0.250 | 0.334 | 2416.30 | 1724.27 |
| 410 | 149.85 | 0.642 | 119.15 | 4841.59 | 0.250 | 0.336 | 2556.73 | 1812.28 |
| 420 | 154.54 | 0.652 | 119.19 | 5079.15 | 0.250 | 0.337 | 2697.32 | 1899.28 |
| 430 | 162.75 | 0.672 | 119.26 | 5505.59 | 0.250 | 0.340 | 2953.59 | 2055.02 |
| 440 | 170.63 | 0.702 | 119.37 | 6135.22 | 0.250 | 0.343 | 3341.26 | 2284.02 |
| 450 | 174.36 | 0.732 | 119.49 | 6738.80 | 0.251 | 0.346 | 3723.57 | 2502.50 |
| 460 | 175.90 | 0.756 | 119.58 | 7190.84 | 0.251 | 0.349 | 4016.88 | 2665.48 |
| 470 | 176.48 | 0.773 | 119.64 | 7498.73 | 0.251 | 0.351 | 4220.16 | 2776.19 |
| 480 | 176.71 | 0.784 | 119.68 | 7706.84 | 0.251 | 0.352 | 4359.18 | 2850.88 |
| 490 | 176.82 | 0.793 | 119.72 | 7853.95 | 0.251 | 0.352 | 4458.24 | 2903.61 |
| 500 | 176.90 | 0.799 | 119.74 | 7963.93 | 0.251 | 0.353 | 4532.74 | 2943.00 |
| 510 | 176.97 | 0.804 | 119.76 | 8050.23 | 0.251 | 0.354 | 4591.45 | 2973.88 |
| 520 | 177.01 | 0.808 | 119.77 | 8120.51 | 0.251 | 0.354 | 4639.43 | 2999.02 |
| 530 | 177.04 | 0.812 | 119.79 | 8179.34 | 0.251 | 0.354 | 4679.72 | 3020.06 |
| 540 | 177.06 | 0.815 | 119.80 | 8229.66 | 0.251 | 0.354 | 4714.26 | 3038.04 |
| 550 | 177.08 | 0.817 | 119.81 | 8273.41 | 0.251 | 0.355 | 4744.35 | 3053.68 |
| 560 | 177.08 | 0.820 | 119.82 | 8312.01 | 0.251 | 0.355 | 4770.95 | 3067.46 |
| 570 | 177.09 | 0.822 | 119.82 | 8346.45 | 0.251 | 0.355 | 4794.73 | 3079.76 |
| 580 | 176.84 | 0.824 | 119.83 | 8377.44 | 0.251 | 0.355 | 4816.15 | 3090.83 |
| 590 | 167.34 | 0.825 | 119.83 | 8392.48 | 0.251 | 0.355 | 4826.56 | 3096.20 |
| 600 | 150.14 | 0.825 | 119.83 | 8393.14 | 0.251 | 0.355 | 4827.02 | 3096.43 |
| 610 | 129.39 | 0.825 | 119.83 | 8393.14 | 0.251 | 0.355 | 4827.02 | 3096.43 |
| 620 | 106.91 | 0.825 | 119.83 | 8393.14 | 0.251 | 0.355 | 4827.02 | 3096.43 |
| 630 | 83.50 | 0.825 | 119.83 | 8393.14 | 0.251 | 0.355 | 4827.02 | 3096.43 |
| 640 | 59.56 | 0.825 | 119.83 | 8393.14 | 0.251 | 0.355 | 4827.02 | 3096.43 |
| 650 | 41.32 | 0.825 | 119.83 | 8393.14 | 0.251 | 0.355 | 4827.02 | 3096.43 |
| 660 | 32.41 | 0.825 | 119.83 | 8393.14 | 0.251 | 0.355 | 4827.02 | 3096.43 |
| 670 | 27.76 | 0.825 | 119.83 | 8393.14 | 0.251 | 0.355 | 4827.02 | 3096.43 |
| 680 | 25.13 | 0.825 | 119.83 | 8393.14 | 0.251 | 0.355 | 4827.02 | 3096.43 |
| 690 | 23.52 | 0.825 | 119.83 | 8393.14 | 0.251 | 0.355 | 4827.02 | 3096.43 |
| 700 | 22.56 | 0.825 | 119.83 | 8393.14 | 0.251 | 0.355 | 4827.02 | 3096.43 |




(a) Temperature.




(b) Degree of cure.

**Fig. 22.** Temperature and degree of cure along the thickness at different times and in P1 and P2 for the case of non-homogeneous heated plate.

3D temperature distributions and the degree of cure on process-induced defects, such as residual stresses and spring-in angles.

## CRediT authorship contribution statement

**E. Zappino:** Writing – review & editing, Supervision, Methodology, Conceptualization. **M. Santori:** Writing – original draft, Validation, Methodology, Investigation, Formal analysis, Conceptualization. **N. Zobeiry:** Writing – review & editing, Supervision, Methodology, Conceptualization. **M. Petrolo:** Writing – review & editing, Supervision, Project administration, Methodology, Investigation, Funding acquisition, Conceptualization.

## Declaration of competing interest

The authors declare that they have no known competing financial interests or personal relationships that could have appeared to influence the work reported in this paper.

## Acknowledgments

This work was partly supported by the Italian Ministry of Foreign Affairs and International Cooperation, grant number US23GR12.

## Appendix A. Temperature and degree of cure profiles

Fig. 22 shows the temperature and degree of cure along the thickness at different times and in P1 and P2 for the case of non-homogeneous heated plate.

## Appendix B. Evolution of sandwich properties

Tables 9 and 10 show the evolution of the properties of the AS4/8552 material of the sandwich structure at points 2 and 5, respectively. L indicates the fiber direction, while Z and X indicate the through-the-thickness and transverse directions, respectively.

## Data availability

Data will be made available on request.

## References

Al-Dhaheri, M., Khan, K.A., Umer, R., Van Liempt, F., Cantwell, W.J., 2020. Process-induced deformation in U-shaped honeycomb aerospace composite structures. Compos. Struct. 248, 112503.
Baker, A.A., Scott, M.L., 2016. Composite Materials for Aircraft Structures. American Institute of Aeronautics and Astronautics, Inc..
Bathe, K.J., 2006. Finite Element Procedures. Klaus-Jurgen Bathe.
Belingardi, G., Cavatorta, M., Duella, R., 2003. Material characterization of a composite–foam sandwich for the front structure of a high speed train. Compos. Struct. 61 (1–2), 13–25.
Bogetti, T.A., 1989. Process-Induced Stress and Deformation in Thick-Section Thermosetting Composites (Ph.D. thesis). University of Delaware.
Bogetti, T.A., Gillespie, Jr., J.W., 1992. Process-induced stress and deformation in thick-section thermoset composite laminates. J. Compos. Mater. 26 (5), 626–660.
Carrera, E., Cinefra, M., Petrolo, M., Zappino, E., 2014. Finite Element Analysis of Structures Through Unified Formulation. John Wiley & Sons.
Carrera, E., Elishakoff, I., Petrolo, M., 2021. Who needs refined structural theories? Compos. Struct. 264, 113671.
Chen, W., Zhang, D., 2019. Improved prediction of residual stress induced warpage in thermoset composites using a multiscale thermo-viscoelastic processing model. Compos. A 126, 105575.
Ersoy, N., Garstka, T., Potter, K., Wisnom, M.R., Porter, D., Clegg, M., Stringer, G., 2010a. Development of the properties of a carbon fibre reinforced thermosetting composite through cure. Compos. A 41 (3), 401–409.
Ersoy, N., Garstka, T., Potter, K., Wisnom, M.R., Porter, D., Stringer, G., 2010b. Modelling of the spring-in phenomenon in curved parts made of a thermosetting composite. Compos. A 41 (3), 410–418.
Fernlund, G., Mobuchon, C., Zobeiry, N., 2018. 2.3 autoclave processing. In: Beaumont, Peter W.R., Zweben, Carl H. (Eds.), Comprehensive Composite Materials II. Elsevier, Oxford, pp. 42–62.
Fernlund, G., Osooly, A., Poursartip, A., Vaziri, R., Courdji, R., Nelson, K., George, P., Hendrickson, L., Griffith, J., 2003. Finite element based prediction of process-induced deformation of autoclaved composite structures using 2D process analysis and 3D structural analysis. Compos. Struct. 62 (2), 223–234.
Fernlund, G., Rahman, N., Courdji, R., Bresslauer, M., Poursartip, A., Willden, K., Nelson, K., 2002. Experimental and numerical study of the effect of cure cycle, tool surface, geometry, and lay-up on the dimensional fidelity of autoclave-processed composite parts. Compos. A 33 (3), 341–351.
Fisher, A., Levy, A., Kratz, J., 2023. Effects of heat transfer coefficient variations on composite curing. J. Compos. Mater. 57 (3), 363–376.
Ilcewicz, L.B., Smith, P.J., Hanson, C.T., Walker, T.H., Metschan, S.L., Mabson, G.E., Wilden, K.S., Flynn, B.W., Scholz, D.B., Polland, D.R., et al., 1997. Advanced Technology Composite Fuselage: Program Overview. Technical Report.
Johnston, A.A., 1997. An Integrated Model of the Development of Process-Induced Deformation in Autoclave Processing of Composite Structures (Ph.D. thesis). University of British Columbia.
Johnston, A., Vaziri, R., Poursartip, A., 2001. A plane strain model for process-induced deformation of laminated composite structures. J. Compos. Mater. 35 (16), 1435–1469.
Kappel, E., 2015. Spring-in of curved CFRP/foam-core sandwich structures. Compos. Struct. 128, 155–164.

Leijten, J., Bersee, H.E.N., Bergsma, O.K., Beukers, A., 2009. Experimental study of the low-velocity impact behaviour of primary sandwich structures in aircraft. Compos. A 40 (2), 164–175.

Li, Y., Yang, A., Liu, Y., Gao, Y., Zhou, J., Dong, Y., Zhu, S., 2025. Analysis of warping defect formation mechanisms in hot molding of CF/PEEK thin-wall structures and their influence on mechanical properties. Thin-Walled Struct. 207, 112740.

Loos, A.C., Springer, G.S., 1983. Curing of epoxy matrix composites. J. Compos. Mater. 17 (2), 135–169.

Maréchal, Quentin, Ichchou, Mohamed, Berthel, Bruno, Salvia, Michelle, Fossat, Pascal, Bareille, Olivier, Chabchoub, Mohamed, 2025. Composite structures spring back, modeling and sensitivity analysis. Compos. Sci. Technol. 111371.

Mezeix, L., Seman, A., Nasir, M.N.M., Aminanda, Y., Rivai, A., Castanié, B., Olivier, P., Ali, K.M., 2015. Spring-back simulation of unidirectional carbon/epoxy flat laminate composite manufactured through autoclave process. Compos. Struct. 124, 196–205.

Nagaraj, M.H., Shah, S.P., Sabato, A., Maiaru, M., 2024. Validation and verification of a novel higher-order FE framework for process modeling of thermoset composites. Compos. B 279, 111447.

Qiao, W., Yao, W., 2020. Modelling of process-induced deformation for composite parts considering tool-part interaction. Materials 13 (20), 4503.

Ren, M., Wang, Q., Cong, J., Chang, X., 2018. Study of one-dimensional cure simulation applicable conditions for thick laminates and its comparison with three-dimensional simulation. Sci. Eng. Compos. Mater. 25 (6), 1197–1204.

Schoenholz, C., Zappino, E., Petrolo, M., Zobeiry, N., 2024. Efficient analysis of composites manufacturing using multi-fidelity simulation and probabilistic machine learning. Compos. B 280, 111499.

Stringer, L.G., 1989. Optimization of the wet lay-up/vacuum bag process for the fabrication of carbon fibre epoxy composites with high fibre fraction and low void content. Composites 20 (5), 441–452.

Traiforos, N., Matveev, M., Chronopoulos, D., Turner, T., 2023. Spring-in of composite L-shape specimens: An experimental and numerical investigation. Compos. Struct. 310, 116772.

Twigg, G., Poursartip, A., Fernlund, G., 2004a. Tool–part interaction in composites processing. Part I: experimental investigation and analytical model. Compos. A 35 (1), 121–133.

Twigg, G., Poursartip, A., Fernlund, G., 2004b. Tool–part interaction in composites processing. Part II: numerical modelling. Compos. A 35 (1), 135–141.

Wang, B., Fan, S., Chen, J., Yang, W., Liu, W., Li., Y., 2023. A review on prediction and control of curing process-induced deformation of continuous fiber-reinforced thermosetting composite structures. Compos. A 165, 107321.

White, S.R., Hahn, H.T., 1992a. Process modeling of composite materials: residual stress development during cure. Part I. Model formulation. J. Compos. Mater. 26 (16), 2402–2422.

White, S.R., Hahn, H.T., 1992b. Process modeling of composite materials: residual stress development during cure. Part II. Experimental validation. J. Compos. Mater. 26 (16), 2423–2453.

Zappino, E., Masia, R., Zobeiry, N., Petrolo, M., Carrera, E., 2024a. Development of mitigation strategies for process-induced deformations through finite elements. Mech. Adv. Mater. Struct. 31 (28), 11054–11066.

Zappino, E., Santori, M., Masia, R., Zobeiry, N., Petrolo, M., 2024b. Numerical analysis of the impact of process parameters on the residual stress of a flat composite part. Aerotecnica Missili Spazio 1–15.

Zappino, E., Zobeiry, N., Petrolo, M., Vaziri, R., Carrera, E., Poursartip, A., 2020. Analysis of process-induced deformations and residual stresses in curved composite parts considering transverse shear stress and thickness stretching. Compos. Struct. 241, 112057.

Zhu, Q., Geubelle, P.H., Li, M., Tucker, III, C.L., 2001. Dimensional accuracy of thermoset composites: simulation of process-induced residual stresses. J. Compos. Mater. 35 (24), 2171–2205.

Zobeiry, N., Forghani, A., Li, C., Gordnian, K., Thorpe, R., Vaziri, R., Fernlund, G., Poursartip, A., 2016. Multiscale characterization and representation of composite materials during processing. Philos. Trans. R. Soc. A 374 (2071), 20150278.

Zobeiry, N., Poursartip, A., 2015. The origins of residual stress and its evaluation in composite materials. In: Structural Integrity and Durability of Advanced Composites. Elsevier, pp. 43–72.